Applied Catalysis B: Environmental 164 (2015) 18–30

Contents lists available at ScienceDirect

Applied Catalysis B: Environmental

journal homepage: www.elsevier.com/locate/apcatb

The catalytic methanation of coke oven gas over Ni-Ce/Al_2O_3 catalysts prepared by microwave heating: Effect of amorphous NiO formation

Zhifeng Qin, Jun Ren*, Maoqian Miao, Zhong Li, Jianying Lin, Kechang Xie

Key Laboratory of Coal Science and Technology, Taiyuan University of Technology, Ministry of Education and Shanxi Province, Taiyuan 030024, China

ARTICLE INFO

Article history:
Received 5 May 2014
Received in revised form 1 August 2014
Accepted 31 August 2014
Available online 6 September 2014

Keywords:
Coke oven gas
Microwave heating
Methanation
Nickel based catalysts
Hydrogen-pulse chemisorption

ABSTRACT

Ni-Ce/γ-Al_2O_3 catalysts were prepared by traditional and microwave heating and tested by the methanation of simulated coke oven gas in a fixed bed reactor. Various characterization techniques were used to examine the bulk and surface properties of the catalysts. The catalysts obtained by microwave heating show superior methanation activity to traditional catalysts. Conversion of 100% CO, CO_2, and O_2, with part conversion of C_2H_6, was obtained on the MO-15NC catalyst with the following reaction conditions: 260 °C, 3.0 MPa and 20,000 mL g^{-1} h^{-1} weight hourly space velocity. The temperature gradient between the NiO and the alumina support caused by the difference in microwave energy absorption promotes the formation of a large amount of highly dispersed amorphous NiO with a Ni loading of less than 15 wt%, and is more active for the methanation reaction because of a weak interaction with the support, large active surface area and low CO dissociation energy.

1. Introduction

The global demand for energy is constantly on the rise because of population explosion, rapid urbanization, and industrial growth. Existing energy resources are becoming insufficient to cope with current energy requirements. We should therefore not only explore the potential for using alternative renewable energies but also utilize available energy resources to their maximum potential. Coke oven gas (COG) is highly rated as a valuable by-product of coal carbonization to produce coke in the steel industry [1]. COG is a combustible gas mixture, consisting mainly of ~55–60% H_2, ~23–27% CH_4, ~5–9% CO, ~1.9–4% CO_2, ~3–5% N_2, and ~0.4–0.8% O_2 along with other hydrocarbons, H_2S and NH_3 in small quantities [2]. A huge quantity of coke gas is available as a byproduct of the coke-making industry in China [3]. In 2012, the coke output of China was more than 436 million tons. Since each ton of coke produces 430 Nm^3 COG in the coking process, the annual yield of COG amounts to 187.5 billion Nm^3 [4]. In recent years, research and development into technologies that use COG have made it a highly commercial and profitable industry in China. Currently, ~80–90% of COG is employed as fuel for coke ovens, the synthetic industry, in the generation of electricity, and also by thousands of families. Approximately 20 billion Nm^3 of surplus COG is burnt in torches or emitted directly into the air in 2012. This results in a considerable waste of resources and the acceleration of environmental destruction [5–7]. There is an urgent demand for the development of new technologies to utilize COG in the coking industry.

Considerable effort has been made to produce syngas from COG by partial oxidation [3,4,8–10], steam reforming [9–12] or CO_2 reforming [2,6,7,10,13]. However, a great deal of energy input is required for the reforming process, which reduces overall energy efficiency. Recently, the production of synthetic natural gas (SNG) via methanation of COG has been suggested [5,14]. This would result in a saving of resources and an improvement in energy efficiency. Using the example of China, the greatest need is to produce more natural gas [15], demand for which is expected to grow by more than a factor three in a few years. Thus, natural gas synthesized from COG can provide only a supplement to China's natural gas market.

The methanation of COG to SNG is a catalytic process so it is very important to develop appropriate catalysts for the new process. A large number of papers [16–24] report the use of Ni/Al_2O_3 catalysts for the methanation reaction, because the Al_2O_3 support possess chemical and physical stability and high mechanical resistance. CeO_2 [16] was often employed as structural and electronic promoter to promote the dispersion of metallic Ni on the support and change the properties of metal Ni through strong metal to support interactions. These studies were mainly concerned with the methanation reactions of simple mixtures of carbon monoxide and carbon dioxide with air. In contrast, there have been no

* Corresponding author at: No. 79 Yingze West Street, Taiyuan 030024, China. Tel.: +86 351 6018598; fax: +86 351 6018598.
E-mail address: renjun@tyut.edu.cn (J. Ren).

http://dx.doi.org/10.1016/j.apcatb.2014.08.047
0926-3373/

Table 1
The preparation conditions of various Ni-Ce/Al_2O_3 catalysts.

Sample	Ni loading (wt%)	Ce loading (wt%)	Calcination methods	Calcination conditions		
				Atmosphere	Temperature (°C)	Time (min)
MO-5NC	5	5	Microwave oven	Nitrogen	450	60
MO-10NC	10	5	Microwave oven	Nitrogen	450	60
MO-15NC	15	5	Microwave oven	Nitrogen	450	60
MO-20NC	20	5	Microwave oven	Nitrogen	450	60
MF-15NC	15	5	Muffle furnace	Air	450	60
TF-15NC	15	5	Tubular furnace	Nitrogen	450	60

studies of the methanation reaction of COG with a more complex composition.

The focus of increased research into methanation catalysts has been mostly on group VIII metals such as Ni [25–28], Ru [25,29], Rh [30], Pd [31] and Pt [32] supported on diverse materials. Among these, Ni-based catalysts have been investigated extensively for industrial purposes because nickel is inexpensive and readily available. However, conventional Ni catalysts supported on alumina are easily deactivated as a result of being prone to carbon deposition. Interest has therefore been focused on noble metal-based catalysts owing to their high activity, selectivity, and strong carbon deposition resistance. Despite these advantages, expensive prices have restricted their widespread application. Bimetallic catalysts, which comprise Ni and another metal, are promising as a priority of study from an economical and theoretical perspective, because they are more active than traditional monometallic catalysts and could reduce the amounts required as well as the cost of the precious catalysts.

Microwave heating has attracted much attention in the preparation of catalysts since it causes rapid and even heating, leading to uniform distribution of the active components in the support. In addition, it can alter the activity and selectivity in certain reactions [33]. In this work, Ni-Ce/γ-Al_2O_3 catalysts were prepared by conventional and microwave assisted heating and used in the catalytic methanation of both CO and CO_2 (both present in coke oven gas) in a fixed-bed reactor. The catalysts were characterized by powder X-ray diffractometry (XRD), hydrogen temperature-programmed reduction (H_2-TPR), hydrogen pulse chemisorption, temperature-programmed surface reaction (TPSR) and transmission electron microscopy (TEM). The results indicate that microwave heating promotes the formation of the NiO species interacting weakly with the γ-alumina support, increases the metal active surface area and leads to improved catalytic activity.

2. Experimental

2.1. Catalyst preparation

The Ni-Ce/Al_2O_3 catalysts were prepared as follows. γ-Al_2O_3 (236.64 $m^2\,g^{-1}$, 1.23 $g\,cm^{-3}$, China Research Institute of Daily Chemical Industry, Taiyuan, China) was added to an aqueous solution containing an appropriate amount of cerium nitrate and nickel nitrate (both ≥99.0%, Sinopharm Chemical Reagent Co. Ltd., Beijing, China). The mixture was then maintained at 70 °C for 4 h with stirring. The products were dried overnight at 70 °C in air and calcined at 450 °C for 60 min under a N_2 atmosphere in a microwave oven (NJZ4-3, Nanjing Jiequan Microwave Equipment Co. Ltd., Nanjin, China). The specific process of microwave calcination has been described in detail in a previous publication by this group [33]. The resulting catalysts *x*Ni-5Ce/γ-Al_2O_3 (*x* = 5, 10, 15 and 20), where *x* represents the percentage of Ni with respect to the total catalyst, were denoted as MO-5NC, MO-10NC, MO-15NC and MO-20NC, respectively. For comparison, two other catalysts prepared by calcination of the precursor mixture at 450 °C for 60 min in air in a muffle furnace (SX-4-10, Shanghai Hongji Instrument Co. Ltd., Shanghai, China) and under N_2 atmosphere in a tubular furnace (GSL-1500X, Hefei Kejing Materials Technology Co. Ltd., Hefei, China) were denoted MF-15NC and TF-15NC, respectively. The details are shown in Table 1.

2.2. Catalyst characterization

2.2.1. XRD characterization

XRD spectra were recorded on a X-ray diffractometer (Rigaku D/Max 2500, Rigaku Industrial Co., Tokyo, Japan), with CuKα as X-ray source (λ = 1.54056 Å, 40 kV, 100 mA). Spectra were recorded over a 2θ range of 10–80° at 4° min^{-1}. The crystallite size of the NiO was determined by X-ray line broadening analysis for NiO (3 1 1) spinel peaks from the Scherrer–Warren equation:

$$d_{(XRD)} = \frac{\kappa\lambda}{\beta\cos\theta} \quad (1)$$

where κ is the particle shape factor, taken as 0.94, and λ is 1.5418 Å. The measured half width '*B*' was corrected for the instrumental line broadening '*b*' using $\beta = B - b$. The instrumental line broadening '*b*' was determined from a silicon reference supplied by Rigaku and was 0.055°. In general, the maximum grain size that can be measured by XRD is 1000 Å, and $d_{(XRD)}$ only represents the crystalline size of the normal to crystal surface direction, which is independent of other directions.

2.2.2. H_2-TPR characterization

H_2-TPR measurements were carried out on a chemisorption analyzer (AutoChem II 2920, Micromeritics Instrument Co., Atlanta, Georgia, USA) using the following steps. Firstly, 80 mg of sample was placed in a quartz U-tube reactor which was purged in Ar at 300 °C for 30 min and then cooled to ambient temperature. The catalyst was then heated at 10 °C min^{-1} to 750 °C with a gas mixture of 10% H_2 (Ar as balance) at a flow rate of 20 mL min^{-1}. The hydrogen consumption was monitored using a thermal conductivity detector (TCD).

2.2.3. H_2 pulse chemisorption characterization

H_2 pulse chemisorption of catalysts was performed using a Micrometrics AutoChem II 2920. Prior to reduction, 80 mg sample was placed in a quartz U-tube reactor and each catalyst was reduced at 450 °C in pure H_2 (99.99%) for 60 min. The sample was then purged in Ar (99.999%) at 500 °C for 60 min and cooled to 30 °C in flowing Ar. Finally, hydrogen plus chemisorption was initiated by holding the catalysts at 30 °C using 10% H_2/Ar and pulsing 20 times to adsorption saturation. Hydrogen desorption was monitored using a TCD. H_2 uptakes at monolayer coverage of the Ni crystallites were used to estimate Ni dispersion and metallic surface area, assuming that each surface Ni atom chemisorbs one hydrogen atom ($H/Ni_{surface} = 1$). The nickel metal dispersion, nickel surface

area, active nickel surface areas and average nickel particle size are calculated from Eqs. (2)–(5), respectively:

$$D_{Ni} = S_f \times \frac{V_{ads}}{V_g} \times \frac{M}{wt\%} \times 100\% \times 100\% \quad (2)$$

$$S_{cat} = S_f \times \frac{V_{ads}}{V_g} \times N_a \times \sigma_m \times \frac{m^2}{10^{18}\ nm^2} \quad (3)$$

$$S_{Ni} = S_f \times \frac{V_{ads}}{V_g} \times \frac{100\%}{wt\%} \times N_a \times \sigma_m \times \frac{m^2}{10^{18}\ nm^2} \quad (4)$$

$$d_{HOT} = \frac{F_g}{\rho \times S_{Ni}} \times \frac{m^3}{10^6\ cm^3} \times \frac{10^9\ nm}{m} \quad (5)$$

where S_f is the stoichiometry factor; V_g is the molar volume of gas at STP, 222,414 mL mol^{-1}; M is the molecular weight of the metal, a.u.; V_{ads} is the volume adsorbed, mL g^{-1}; wt% is the nickel weight percentage in the sample, %; σ_m is the area of active metal atom, nm^2; N_a is Avogadro's constant, 6.023×10^{23} molecules·mol^{-1}; F_g is the crystallite geometry factor (hemisphere = 6, cube = 5); and ρ is the specific gravity of the metal, g mL^{-1}.

2.2.4. TPSR characterization

TPSR was carried out using a Micrometrics AutoChem II 2920. The catalyst was first reduced at 450 °C in H_2 for 60 min, cooled to room temperature and then exposed to pure CO for 30 min. The catalyst was then purged in Ar for 60 min, and heated at a rate of 10 °C min^{-1} to 500 °C with 10 vol% H_2 (Ar as balance) at a flow rate of 20 mL min^{-1}. The gases desorbed from the catalyst during TPSR were monitored on-line using a quadrupole mass spectrometer (QIC 20, Hiden Analytical Ltd., Warrington, England), equipped with a variable-leak valve. The amounts of desorption of CO (m/e = 28), and CH_4 (m/e = 16) were calculated by calibration curves for each gas.

2.2.5. TEM characterization

TEM analysis was conducted using a transmission electron microscope (JEM-2100F, Japan Electron Optics Laboratory Ltd., Tokyo, Japan), operating at an acceleration voltage of 200 keV. The catalyst powders were dispersed in ethanol and two drops of the solution were transferred to a carbon/Cu grid (300 Mesh). Grids were allowed to dry before TEM characterization.

2.2.6. X-ray photoelectron spectroscopy characterization

X-ray photoelectron spectroscopy (XPS) data were acquired on an ESCALab 250Xi electron spectrometer (Thermo Electron Instruments Co., Ltd., Massachusetts, USA) using Mg K_α radiation (1253.6 eV). Binding energies were calibrated relative to the C1s peak from carbon contamination at 284.6 eV. The introduction chamber of the spectrometer was located in a glove box for the preparation of the reduced samples, which were transferred under inert atmosphere.

2.3. Catalyst activity test

The methanation of simulated COG was carried out in a stainless steel high-pressure fixed bed reactor (Φ12 mm × 2 mm × 500 mm). 0.50 g of catalyst was placed in the center of the reactor (the constant temperature region), and reduced at 450 °C for 2 h. The furnace temperature was allowed to fall to reaction temperatures and then the coke oven gas was introduced into the system. After stable reaction for 1 h, the effluent of the reactor consisted of H_2, CO_2, CO, N_2, CH_4 and C_2H_6, as well as H_2O. H_2O was removed from the exit gas through a cold trap and a dryer, while the dry gas entered an on-line gas chromatograph (GC-950, Shanghai Haixin Chromatograph Instrument Co., Ltd, Shanghai, China) equipped with TCD and FID detectors for analyzing its composition. H_2, O_2, N_2, CO, CH_4 and CO_2 were separated using a 2-m carbon molecular sieve (TDX-1) column with carrier gas helium (99.999 vol.%) and a TCD detector at an oven temperature of 60 °C. CH_4 and C_2H_6 were separated using a 1-m GDX-502 with carrier gas helium (99.999 vol.%) and FID detector at an oven temperature of 60 °C. The turnover frequency (TOF) of a catalyst is defined as the number of reactant molecules converted to products over one active catalyst site per second. In this case, each Ni atom on the outer surface of the Ni particles is considered to be an active site [34]. The conversions of CO_2 and CO, the yield of CH_4 and the TOF of the Ni/support catalysts were calculated using Eqs. (6)–(9):CO conversion (X_{CO}, %):

$$X_{CO} = \frac{N_{in}y_{CO,in} - N_{out}y_{CO,out}}{N_{in}y_{CO,in}} \times 100\% \quad (6)$$

CO_2 conversion (X_{CO_2}, %):

$$X_{CO_2} = \frac{N_{in}y_{CO_2,in} - N_{out}y_{CO_2,out}}{N_{in}y_{CO_2,in}} \times 100\% \quad (7)$$

TOF of CO and CO_2:

$$TOF\ (s^{-1}) = \frac{X_i \cdot N_{in}y_{i,in} \cdot N_a}{V_g \cdot A} \quad (8)$$

CH_4 yield (Y_{CH_4}, %):

$$Y_{CH_4} = \frac{N_{out}y_{CH_4,out}}{N_{in}(y_{CO,in} + Y_{CO_2,in} + y_{CH_4,in} + 2y_{c_2H_6,in})} \times 100\% \quad (9)$$

where N_{in} or N_{out} denotes the flow rate (mL h^{-1}) at the inlet or outlet and y_{in} or y_{out} represent the molar fraction of carbon oxides or methane at the inlet or outlet; N_a is Avogadro's number; V_g is the molar volume of gas at STP, 222,414 mL mol^{-1}; and A is the number of exposed Ni surface sites (from the calculations in Section 2.2.3).

3. Results

3.1. Catalyst activity test

3.1.1. Effect of temperature

The catalytic activity of the six catalysts was studied from 200 to 400 °C. The results obtained for 20,000 mL g^{-1} h^{-1} and 0.5 MPa are displayed in Fig. 1, where the conversions of the carbon oxides are plotted as a function of reaction temperature. Fig. 1(a) shows that the CO conversion increases with increase of temperature, and is relatively sensitive to the reaction temperature. The catalysts prepared by microwave heating show better catalytic activity than those prepared by conventional heating. CO conversion achieves 100% over the MO-15NC and MO-20NC samples above 240 °C. For MO-5NC and MO-10NC, CO is completely converted above 300 °C. However, the CO conversion over MF-15NC and TF-15NC did not reach 100% until the reaction temperature was raised to 360 °C. Fig. 1(b) shows that CO_2 conversion also increases with increasing temperature but at a slower rate compared with that of CO conversion. Except for MO-15NC, CO_2 conversions over the other five catalysts are below 80%, and CO_2 conversions over TF-15NC and MF-15NC are less than 35% at temperatures below 300 °C. These results can probably be attributed to the complex composition of COG. In the methanation of COG, the low activity sites of the Ni-Ce/γ-Al_2O_3 catalysts are first occupied by the CO dissociation, because higher energy is needed for the CO_2 dissociation in the methanation reaction.

3.1.2. Effect of space velocity

The effect of weight hourly space velocity (WHSV) on the methanation of COG has been studied in the range 20,000–40,000 mL g^{-1} h^{-1}. Typical results obtained below 260 °C and 0.5 MPa over the four catalysts are depicted in Fig. 2. Fig. 2(a)

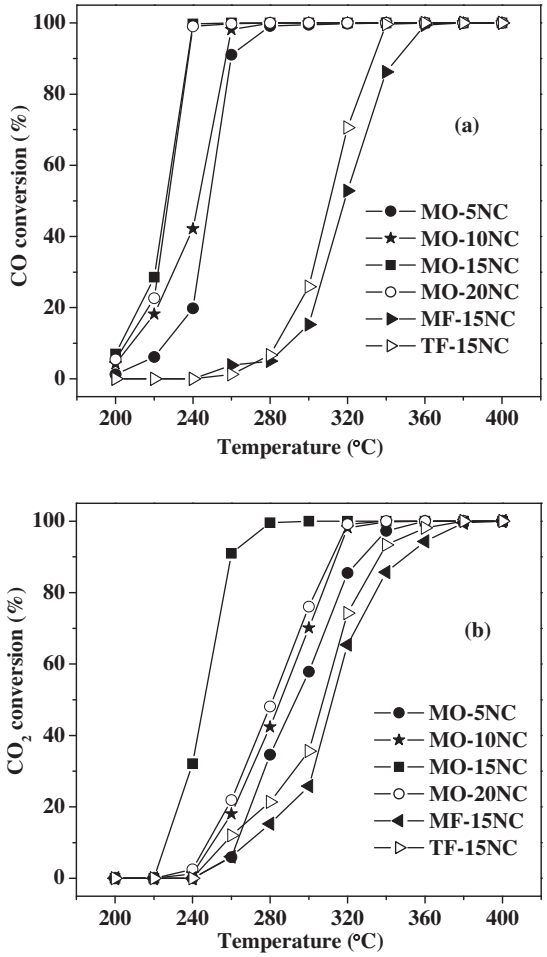

Fig. 1. Effect of reaction temperature on (a) carbon monoxide conversion and (b) carbon dioxide conversion over different catalysts. Reaction conditions: WHSV = 20,000 mL g^{-1} h^{-1}, P = 0.5 MPa.

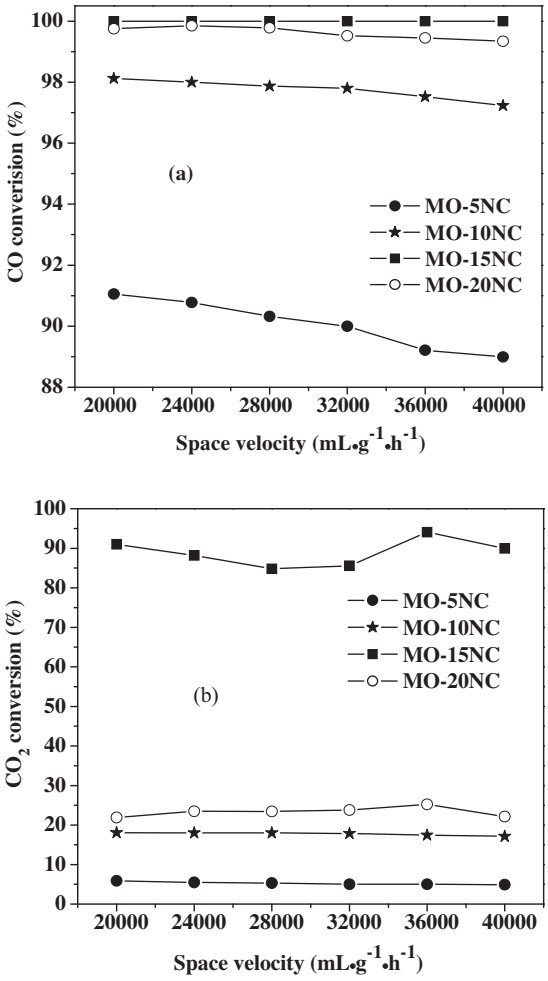

Fig. 2. Effect of space velocity on (a) carbon monoxide conversion and (b) carbon dioxide conversion over different catalysts. Reaction conditions: T = 260 °C, P = 0.5 MPa.

shows that CO conversion decreases slightly over MO-5NC, MO-10NC and MO-20NC catalysts with increase of the space velocity. However, the CO conversion over MO-15NC remains at 100% over the range 20,000–40,000 mL g^{-1} h^{-1}.

As can be seen in Fig. 2(b), MO-15NC shows significantly higher catalytic activity for the methanation of CO_2 compared with the other catalysts. The CO_2 conversion is below 30% over MO-5NC, MO-10NC and MO-20NC catalysts but reaches more than 85% over MO-15NC in the range 20,000–40,000 mL g^{-1} h^{-1}. In addition, there is no obvious change in CO_2 conversion over MO-5NC and MO-10NC with increasing space velocity, meaning that the entire catalyst bed works efficiently. However, CO_2 conversion over MO-15NC and MO-20NC reaches maximum values of 94.1% and 25.2%, respectively, at a space velocity of 36,000 mL g^{-1} h^{-1}.

3.1.3. *Effect of pressure*

In this section, the catalytic performances of four catalysts prepared by microwave heating were studied by varying the pressure from 0.5 to 3.0 MPa. The tests were carried out at 260 °C and 20,000 mL g^{-1} h^{-1}. Fig. 3(a) shows that CO conversion increased with increasing reaction pressure. As the reaction pressure is raised from 0.5 to 3.0 MPa, the CO conversion over MO-5NC increases from 91% to 96.5% and reaches 100% over the other catalysts at 2.5 MPa. Fig. 3(b) shows that the CO_2 conversion clearly increases with increasing reaction pressure as compared with that of CO conversion. However, only the CO_2 conversion over MO-15NC reaches close to 100%, when the reaction pressure is raised to 3.0 MPa.

The above results indicate that the heating methods as well as the amounts of NiO loading have significant effects on the active performance of the Ni-Ce/γ-Al_2O_3 catalysts. The methanation of COG over the MO-15NC catalyst was then carried out at 260 °C, 3.0 MPa and 20,000 mL g^{-1} h^{-1}. The chemical compositions of the simulated COG before and after the methanation reaction are shown in Table 2. This reveals that the amounts of CO, CO_2 and O_2 decrease to zero, the amount of C_2H_6 decreases from 2.42% to 1.03%, and the amount of CH_4 increases from 25.80% to 61.55% in the product gases. This indicates that CO, CO_2 and O_2 are completely converted, and C_2H_6 can be partly converted after methanation of the COG.

To develop optimized reaction conditions, the effects of reaction conditions (reaction temperature, space velocity and reaction pressure) on reaction performance have been investigated for all catalysts. The TOF_{CO}, TOF_{CO_2}, and CH_4 yield of all catalysts are listed in Table 3. These values for catalysts prepared by microwave were significantly higher than those from traditional heating. The CH_4 yield agrees well with the trend of active surface areas. Moreover, increasing the Ni loading (>15 wt%) does not necessarily lead to further enhancement in TOF_{CO} and TOF_{CO_2}. Comparing the TOF as calculated for the various catalysts shows no monotonous relationship between intrinsic activity and Ni loading (Table 3).

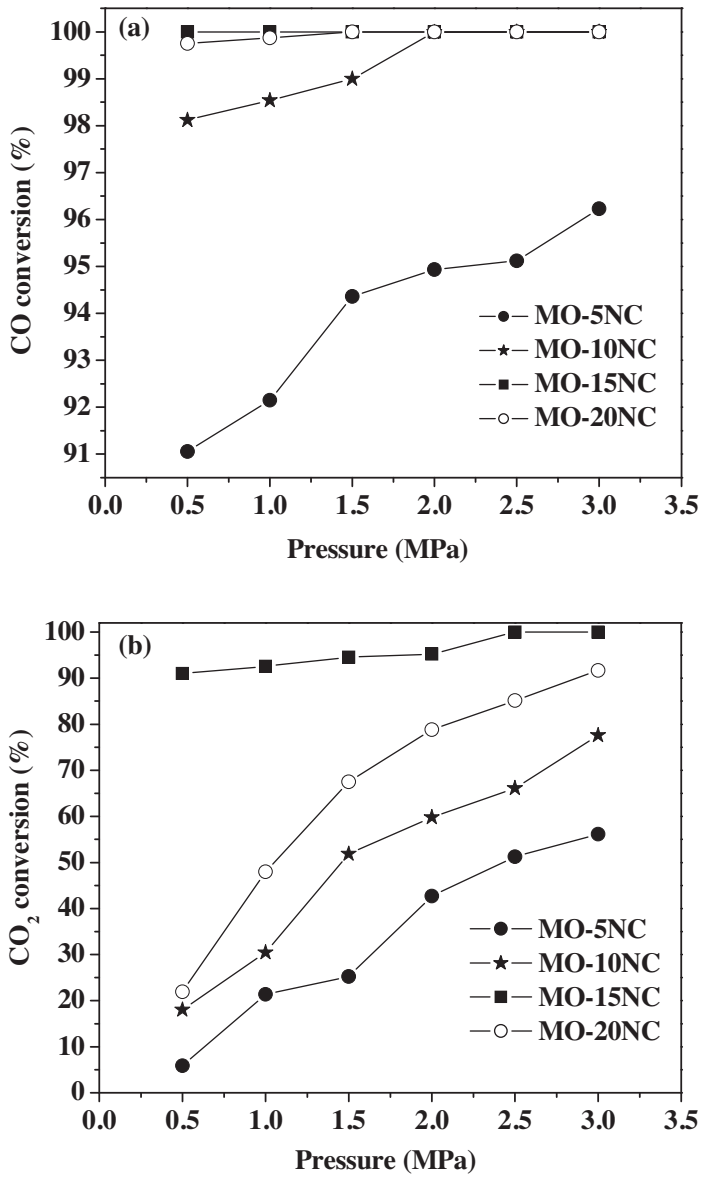

Fig. 3. Effect of pressure on (a) the carbon monoxide conversion and (b) carbon dioxide conversion over different catalysts. WHSV = 20,000 mL g^{-1} h^{-1}, T = 260 °C.

Table 2
Chemical composition of simulated COG and the product after methanation reaction on MO-15NC catalyst.

Name	H_2 (%)	CO (%)	CO_2 (%)	CH_4 (%)	C_2H_6 (%)	N_2 (%)	O_2 (%)
COG	57.46	6.90	2.99	25.80	2.42	3.95	0.48
Products	34.51	0	0	57.70	1.80	5.99	0

Reaction conditions: T = 260 °C, P = 3.0 MPa, WHSV = 20,000 mL g^{-1} h^{-1}.

Table 3
Results of chemisorption and XRD measurements and intrinsic catalytic activities of various Ni-Ce/Al_2O_3 catalysts.

Catalyzer	Ni dispersion (D_{Ni}, %)[a]	S_{Ni} (m^2 g^{-1})[b]	S_{cat} (m^2 g^{-1}_{cat})[c]	d_H (nm)[d]	d_{XRD} (nm)[e]	TOF_{co} (s^{-1})[f]	TOF_{CO_2} (s^{-1})[f]	CH_4 yield[f]
MO-5NC	32.4	266.2	14.1	2.5	8.3	0.0451	0.0029	87.2
MO-10NC	28.1	230.8	23.1	2.9	9.3	0.0281	0.0055	89.5
MO-15NC	25.5	209.9	31.5	3.2	9.9	0.0222	0.0202	95.7
MO-20NC	17.6	144.6	28.9	4.7	11.2	0.0242	0.0053	92.5
TF-15NC	11.4	93.2	13.9	7.2	13.8	0.0021	0.0030	70.7
MF-15NC	10.2	84.5	12.7	8.0	14.4	0.0017	0.0032	72.9

[a] D_{Ni}: the amount of exposed Ni on the surface of the catalysts/the amount of Ni in the catalysts, assuming Ni/H = 1 from Eq. (2).
[b] S_{Ni}: metal surface area per gram of metal from Eq. (4).
[c] S_{cat}: Ni active metal surface area per gram of sample from Eq. (3).
[d] d_H: average grain diameter from Eq. (5).
[e] d_{XRD}: calculated from NiO (3 1 1) plane using Scherrer equation from Eq. (1).
[f] TOF_{co} and TOF_{CO_2} were calculated from Eq. (8), and CH_4 yield was calculated from Eq. (9); reaction conditions: P = 1.0 MPa, WHSV = 20,000 mL g^{-1} h^{-1}, T = 260 °C.

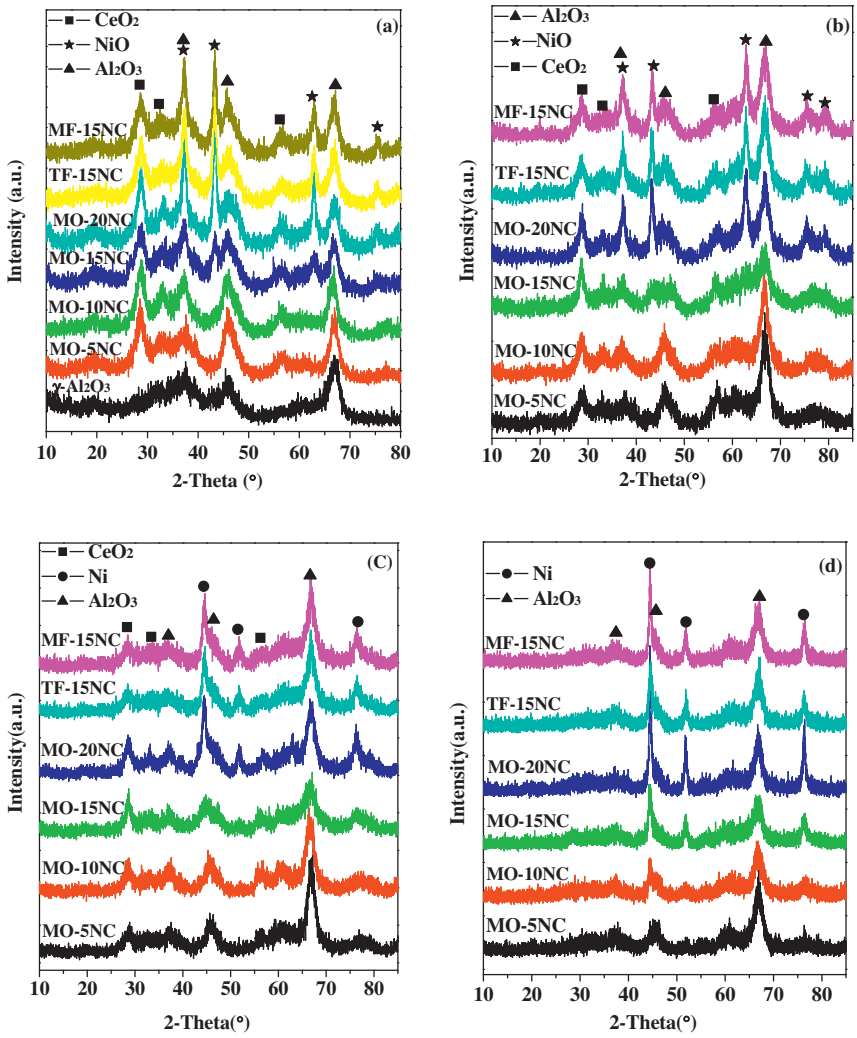

Fig. 4. XRD patterns of different catalysts (a) fresh catalysts, (b) after reduction at 250 °C; (c) after reduction at 500 °C and (d) after reduction at 700 °C.

3.2. Catalyst characterization

3.2.1. XRD analysis

The Ni-Ce/Al_2O_3 catalysts, as well as the support, were characterized by XRD and their patterns are shown in Fig. 4(a). The support is composed of γ-Al_2O_3, confirmed by the peaks on the XRD pattern (JCPDS card No. 10-0425) [18]. For all catalysts, the diffraction peaks at 37.3°, 43.2°, 62.9° and 75.3° are attributed to distinct peaks of cubic NiO (JCPDS card NO. 73-1519) [22], and the diffraction peaks at 28.5°, 33.0°, 47.5° and 56.3° are attributed to distinct peaks of CeO_2 (JCPDS card NO. 65-5923). In addition, no crystal $NiAl_2O_4$ was observed, because the diffraction peaks of γ-Al_2O_3 and $NiAl_2O_4$ probably overlap in the broadened XRD patterns [35].

As seen in Fig. 4(a), the intensity of the NiO peaks of samples containing smaller quantities of Ni (MO-5NC and MO-10NC) were too weak to be identified by XRD; only broad and diffuse lines corresponding to γ-Al_2O_3 are detected [36]. The diffraction peaks of NiO can be clearly seen when the Ni loading increases to 20 wt%. The crystallite sizes of the NiO for different catalysts were calculated from the line width of the NiO (3 1 1) diffraction lines using the Scherrer equation, with the results listed in Table 3. We observe that the average particle size of NiO increases from 8.3 to 11.2 nm and the diffraction peaks of NiO become gradually more intense and sharper with the increase of Ni content from 5 to 20 wt% [22].

Fig. 4 shows that the NiO diffraction peaks of TF-15NC, MF-15NC are clearly more intense than those of MO-15NC. As shown in Table 3, the average NiO particle size in TF-15NC and MF-15NC is larger than that in MO-15NC. These results indicate that microwave heating can result in an ideal dispersion of NiO on the alumina support.

Fig. 4(b)–(d) show the XRD patterns of the catalysts reduced at 250, 500, and 700 °C, respectively. The temperatures were chosen according to different H_2-TPR reduction peaks shown in Fig. 5. The trend in Fig. 4(b) is similar to that in Fig. 4(a), however, the samples reduced at 250 °C indicate poorer characteristic peaks than those that were calcined. This suggests that part of the NiO, which originated from the free state on the surface, was reduced to Ni during this process. As expected, the Ni diffraction peaks became gradually more intense in both Fig. 4(c) and (d), while those of detectable NiO were inconspicuous. The Ni peak intensities in Fig. 4(d) were stronger than those in Fig. 4(c). This is particularly evident for catalyst MO-15NC, where the Ni peak intensities were too weak to identify at 500 °C, but could be detected clearly at 700 °C if reduced. It can be seen from the three figures that the NiO peak intensities decrease, while the Ni peaks increase with increasing reduction temperatures. This illustrates that the amount of detectable crystalline Ni is enhanced, and that the interactions between Ni and the support can be distinguished. Therefore, the Ni species were arranged into three classes according to the different reduction temperatures.

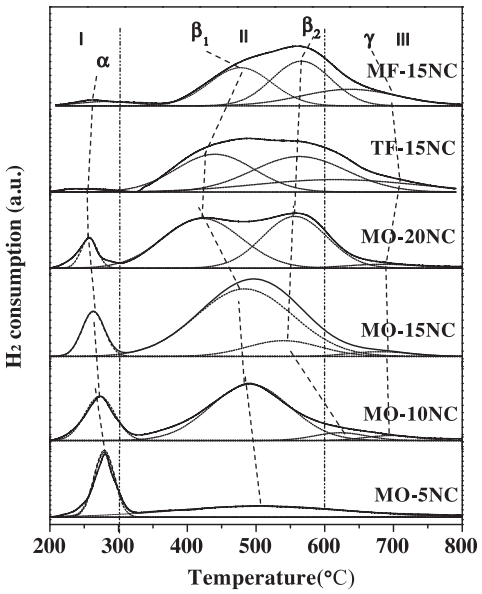

Fig. 5. H_2-TPR profiles of different catalysts.

3.2.2. H_2-TPR analysis

The surface Ni species, reducibility, and metal-support interactions on Ni-Ce/Al_2O_3 catalysts can be characterized by the TPR technique [37]. Fig. 5 shows the TPR profiles of different catalysts. According to previous studies [18,19,22,35–42], overlapping peaks can be deconvoluted using Gaussian-type functions with R^2 higher than 0.99 and the reducible NiO species could be divided into four types: α, β_1, β_2, and γ. Quantitative results for the four NiO species types are listed in Table 4. The α-type NiO in the low-temperature region (T_1 = ~200–300 °C) was assigned to surface amorphous NiO species in the first range. This compound interacted weakly with or did not make contact with the Al_2O_3 support [35,36]. The reduction peaks in the mid-temperature band (T_2 = ~300–600 °C) represents NiO species (β) that interact more strongly with the support than the α-type NiO. These NiO species are believed to result from the NiO precursor in a highly dispersed surface crystal NiO [37,41,42]. As shown in Table 4, the β-type NiO was the main phase in many cases. After a mathematical treatment of the reduction profile, β_1 represents the Ni-rich phase containing some Al^{3+} ions, while β_2 represents the Al-rich phase containing some Ni^{2+} ions [19,36,38]. Correspondingly, in our TPR profiles, the small peak located in the highest-temperature region (T_3 > 600 °C) was assigned to the presence of surface fixed nickel aluminate with spinel structure (γ). This compound has a lower reduction temperature than the $NiAl_2O_4$ crystal phase, because the NiO and alumina-support can form "Ni-O-Al" bonds, but cannot form the $NiAl_2O_4$ crystal phase [35].

As shown in Fig. 5, the reduction temperatures of the catalysts prepared by microwave heating are centered at ~200–300 °C and ~300–600 °C, showing α-type, β_1-type and β_2-type are the main NiO species present. A quantitative analysis of the TPR profiles in Table 4 show that the amount of α-type NiO is larger with lower Ni loadings and the proportion of α-type and β-type NiO reaches more than 50% of the total NiO species. With increasing Ni loading, the content of the easily reducible NiO species gradually decreases. The surface amorphous NiO is probably transformed to NiO phases that either weakly or strongly interact with Al_2O_3. The results reveal that microwave heating promotes the formation of surface amorphous NiO species, and the proportion of the NiO species strongly interacting with the Al_2O_3 support gradually increases with increased Ni loading. However, this finding is inconsistent with the results obtained in previous studies [22–24,36,37], in which the interactions between NiO and the catalyst support decrease with increasing Ni loading for catalysts prepared by conventional heating methods. In fact, different preparation methods merely affect the distribution of Ni species on the Al_2O_3 support. Whether the catalyst is prepared by microwave or in the traditional way, their catalytic behavior is consistent. Therefore, the formation of larger proportions of surface amorphous NiO species leads to a higher catalyst activity.

The reduction temperature of MO-15NC is mostly distributed in the range of ~200–600 °C, but reduction temperatures for TF-15NC and MF-15NC catalysts are mainly scattered at higher temperatures, ~300–750 °C. Apart from β_1-type, β_2 -type and γ-type NiO, α-type NiO is also formed in MO-15NC. The quantitative data in Table 4 shows that α-type and β_1-type NiO account for over 84% of the total for the MO-15NC catalyst. However the percentage of α-type and β_1-type NiO is less than 40% in TF-15NC and MF-15NC. According to the literature [36–38,40], the surface amorphous NiO and the NiO weakly interacting with Al_2O_3 favor the formation of larger Ni particles, which are active at low temperatures. Microwave heating seems to greatly improve the degree of dispersion of the NiO and restrains the migration of the nickel species on the support surface, leading to far lower reduction properties for the NiO species in the Ni-Ce/Al_2O_3 catalysts.

3.2.3. H_2 chemisorption analysis

H_2 chemisorption analysis was performed to determine the metal nickel dispersion, nickel surface area, nickel active surface areas and average particle size of nickel. All were calculated assuming that one hydrogen atom is adsorbed on one surface nickel atom [36,37,43,44]. The results are listed in Table 3. It can be seen that, for the catalysts prepared by microwave heating, the Ni dispersion and metal surface area decrease gradually with increase of Ni loading. In contrast, the average grain size of Ni increases gradually with the increase of Ni loading. This indicates that a highly dispersed Ni species, with smaller particle size, are formed at lower Ni loadings. The active surface area of the catalysts is increased to a maximum ($31.5\ m^2\ g^{-1}{}_{cat}$) and then decreases with further increase of Ni loading, indicating that there is an optimum threshold values of Ni loading.

As shown in Table 3, the active surface areas correlate well with the trend of catalytic activity of the catalysts, as shown in Fig. 1. The Ni dispersion, metal surface area and active surface areas of MO-15NC are double those of TF-15NC and MF-15NC. The MO-15NC catalyst with the largest Ni active surface area shows the optimum catalytic performance in the methanation of COG.

3.2.4. TPSR-MS analysis

TPSR experiments were carried out to ascertain the peak temperature of methane production and carbon monoxide dissociation over the reduced catalysts in the methanation reaction. The peak temperature can be used to explain the different catalytic performances [45]. The hydrogenation of the adsorbed CO results in the formation of one single CH_4 peak [46] and the adsorbed CO appears as one desorption peak during temperature programming, as shown in Fig. 6. The temperature of methane production is usually used as a good measure of the specific activity of the catalyst. However, the temperature of carbon dioxide desorption is used to explain the apparent activation energy for CO dissociation in the hydrogenation process.

As shown in Fig. 6, the methanation temperature on the catalysts prepared by microwave heating at first decreases and then increases as the Ni content increases from 5 wt% to 20 wt%; the lowest methanation temperature for MO-15NC is 187.3 °C. However, catalysts prepared by conventional heating show much higher methanation temperatures, reaching as much as 352.9 °C and 431.0 °C for TF-15NC and MF-15NC, respectively. This result is in good agreement with the trend of active surface areas shown in

Table 4
Gaussian fitting analysis of H_2-TPR patterns of different catalysts.

Sample	Peak area (a.u.)				Fraction of total area (%)			
	α	β_1	β_2	γ	α	β_1	β_2	γ
MO-5NC	16,510.9	23,306.4	70.3	796.8	40.5	57.3	0.2	2.0
MO-10NC	10,130.3	34,023.5	3093.9	1985.5	20.6	69.1	6.3	4.0
MO-15NC	7200.9	46,741.3	8183.4	2053.1	11.2	72.8	12.8	3.2
MO-20NC	4376.9	34,571.3	29,763.7	2498.3	6.2	48.5	41.8	3.5
TF-15NC	1943.2	19,395.9	21,424.7	12,974.2	3.5	34.8	38.4	23.3
MF-15NC	799.8	18,633.8	21,062.1	11,705.5	1.5	35.7	40.4	22.4

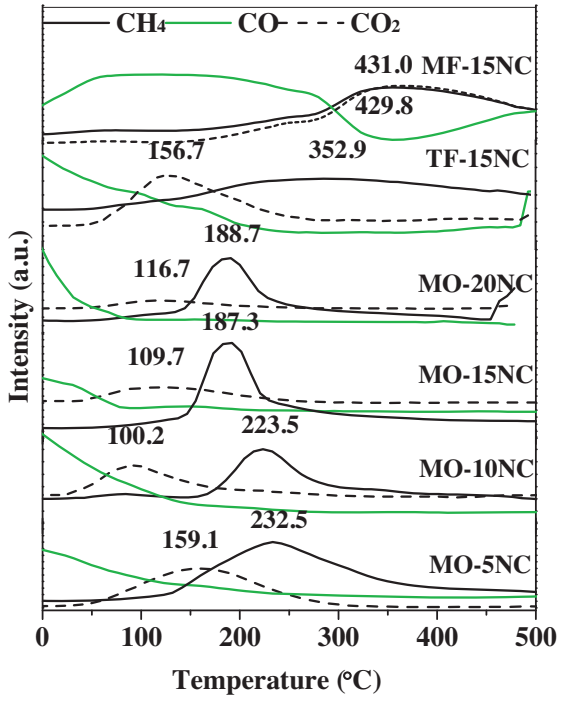

Fig. 6. TPSR-MS profiles of different catalysts.

Table 3 and the catalytic activity shown in Fig. 1. It is well known that metal components in the catalyst play a key role in the dissociation of carbon monoxide to intermediate carbon species in the methanation reaction [47] and the trend observed in the methanation temperatures relates to the changes in active surface areas. It is inferred that the apparent activation energy for CO dissociation will be different, depending on the metallic active sites of the catalysts, leading to different catalytic performance in the methanation reaction. The MO-15NC catalyst, with optimal apparent activation energy for CO dissociation, shows excellent catalytic performance in the methanation reaction. Pre-adsorbed carbon monoxide was desorbed in the form of methane by the reaction with hydrogen. As shown in Fig. 6, the peak temperatures for complete desorption of carbon monoxide from the catalysts prepared by microwave heating are lower than that those prepared by conventional heating. However, they are not completely in accord with the methane temperatures of the above catalysts. It has been reported that the optimal apparent activation energy for CO dissociation will promote the production of intermediate carbon species and methane at low temperature by reaction with hydrogen [48].

As shown in Table 3, catalysts prepared by microwave present a higher active specific surface than those produced by the ordinary heating method, and this contributes to the generation of more active sites. The basic reaction steps of CO methanation [48] are shown as follows:

$$H_2 + 2^* \rightarrow 2H^* \quad (10)$$

$$CO + ^* \rightarrow CO^* \quad (11)$$

$$CO^* + ^* \rightarrow C^* + O^*(RDS) \quad (12)$$

$$C^* + H^* \rightarrow CH^* + ^*(RDS) \quad (13)$$

$$CH^* + H^* \rightarrow CH_2^* + ^*(RDS) \quad (14)$$

$$CO^* + O^* \rightarrow CO_2^* + ^* \quad (15)$$

$$CO_2^* \rightarrow CO_2 + ^* \quad (16)$$

where * denotes an empty active site, C^* is an adsorbed species (e.g., adsorbed carbon) and RDS is the proposed rate-determining step from literature.

The CO desorption and CO_2 and CH_4 generation curves as monitored by mass spectrometer have been shown in Fig. 6. These curves provide extensive comparative information on the two preparations. It can be seen from the reaction mechanism that the reaction rate is limited mainly by the dissociation of CO (Reaction 12) and C hydrogenation (Reactions 13 and 14). Because of the difficulty in detecting intermediate products, the final CO_2 and CH_4 products were used as substitutes to evaluate the apparent activation energy for CO dissociation through the corresponding peak temperature. The peak temperatures on the CO_2 and CH_4 formation and desorption curves reflect the difficulty for CO dissociation and C hydrogenation. The catalysts prepared by microwave have a low temperature CO_2 desorption peak because of their large active specific areas and this is thought to result from the lower CO dissociation temperature and the easier C hydrogenation. In summary, the higher low-temperature methanation activity can be attributed the lower apparent activation energy for CO dissociation on the increased number of active sites of the catalysts prepared by microwave heating.

3.2.5. TEM analysis

TEM images of MF-15NC, TF-15NC and MO-15NC are shown in Fig. 7. A comparison of the images indicates that there are no significant differences in the morphologies of the three catalysts. The TEM micrograph of MO-15NC shows that the NiO particles (black spots) are mainly dispersed in the stratiform γ-Al_2O_3 surfaces, whereas the distribution of NiO particles is inhomogeneous and highly agglomerated in MF-15NC and TF-15NC. For catalysts prepared by microwave heating, the NiO particles cling weakly to the support, which makes it easier to disperse them on to the Al_2O_3 surfaces, but for catalysts prepared by conventional heating, NiO particles bond strongly to the support and some of the particles may be anchored on the Al_2O_3 matrix and coalesce. It appears that microwave heating can restrain agglomeration by preventing migration of the nickel species on the granule surface.

3.2.6. XPS analysis

The bulk analyses presented above, namely H_2-TPR and XRD, reveal the interactions between the active phase nickel oxide and support and nickel crystal structure, respectively. However, these techniques provide no insight into the chemical state of nickel on

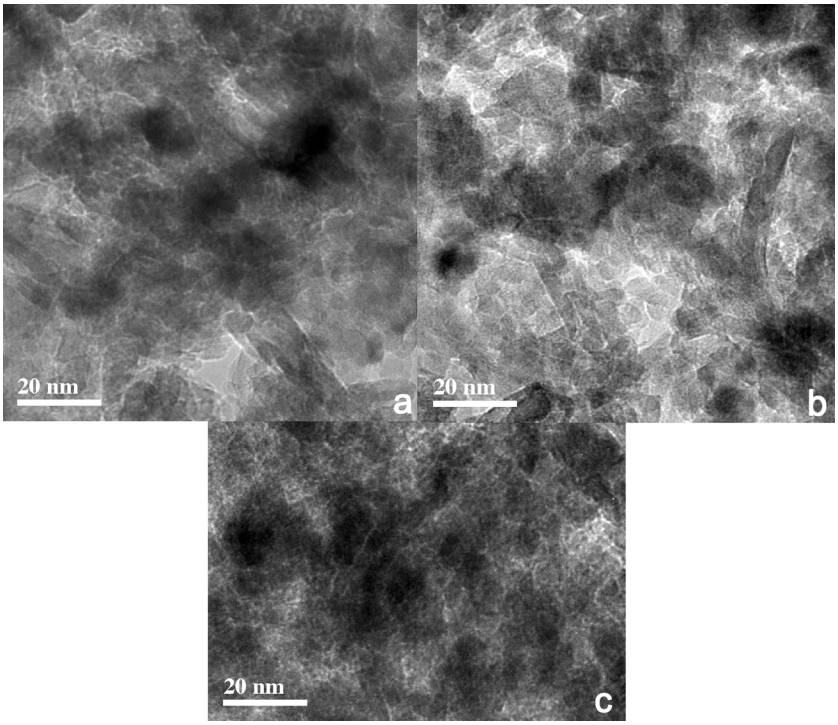

Fig. 7. TEM patterns of different catalysts before reduction (a) TF-15NC; (b) MF-15NC and (c) MO-15NC.

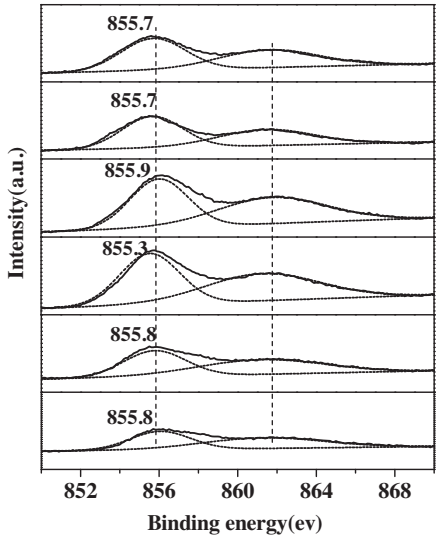

Fig. 8. $Ni2p_{3/2}$ XPS spectra of different catalysts.

the surface [49]. XPS analysis was therefore conducted on different catalysts. The XPS spectra specific to $Ni2p_{3/2}$ of the catalysts are presented in Fig. 8. The $Ni2p_{3/2}$ spectrum was characterized by the elastic peak (BE ~855.5 eV) and the corresponding shake-up satellite at ~6 eV above the principal line [50]. The main peak in the $Ni2p_{3/2}$ spectrum of the catalyst at BE = ~855.5 eV (Fig. 8) indicates the presence of oxidized nickel species (Ni^{2+}). This peak, which is characteristic of Ni^{2+}, is positioned between the binding energy of NiO (854.1 eV [51]) and $NiAl_2O_4$ spinel (856.2 eV [52]). This indicates the intimate interaction of Ni^{2+} and Al^{3+} in the catalyst and the presence of metastable phases intermediate in nature between the two structures [49]. As shown in Fig. 8, the $Ni2p_{3/2}$ BEs of the MO-15NC catalysts are lower than those of the TF-15NC and MF-15NC catalysts. This suggests that weaker interactions exist between Ni and the support on MO-15NC, which is consistent with the TPR results. The intensity of the shake-up satellite in this case is increased gradually with increasing nickel loading because of the presence of extended particles of Ni^{2+} species, which indicate the formation of NiO nanoparticles. This observation correlates with the XRD characterization (Section 3.2.1).

4. Discussion

4.1. Analysis of NiO species

4.1.1. NiO species on alumina-supported nickel catalysts

Nickel catalysts supported on alumina have been used widely in methanation [16–24], reforming [53–61], dehydrogenation [36,38,40,62,63], and hydrogenation [37,49,64] reactions. Previous studies have shown that the formation of NiO species on the alumina support is complex and depends on many factors, such as loading [22–24,36,37,53–56], additives [16–19,36,38–40,56–59,63], crystal type of the support [60,61], calcination temperature [37,49,62], and preparation method [64].

Researchers have found that NiO is formed mainly in the fixed state on the alumina ($NiAl_2O_4$ phase) at a lower Ni loading level. However, the NiO migrates gradually to the surface of the alumina support with increasing Ni loading. This leads to the formation of a NiO phase that can be reduced by hydrogen at a lower temperature [22–24,36,37,53–56].

The introduction of additives into the alumina-supported nickel catalysts can also affect the formation of nickel species. Additives of rare earth metals (Ce [16,38], La [36], Yb [57]), alkaline earth metals (Ca [59], Mg [19,56]), transition metals (Mn [18], Zr [19,63]), and noble metals (Pt [40]) can help reduce the interaction between NiO and alumina. The additive tends to “destroy” the metastable state of the mixed Ni–Al oxide and convey some Ni ions from the Al- to the Ni-rich phase, in the form of Ni-O bond stability. Additives of alkali (K [58]) and transition (Mo [39]) metals can strengthen the interaction mechanism between NiO and alumina, and vice versa.

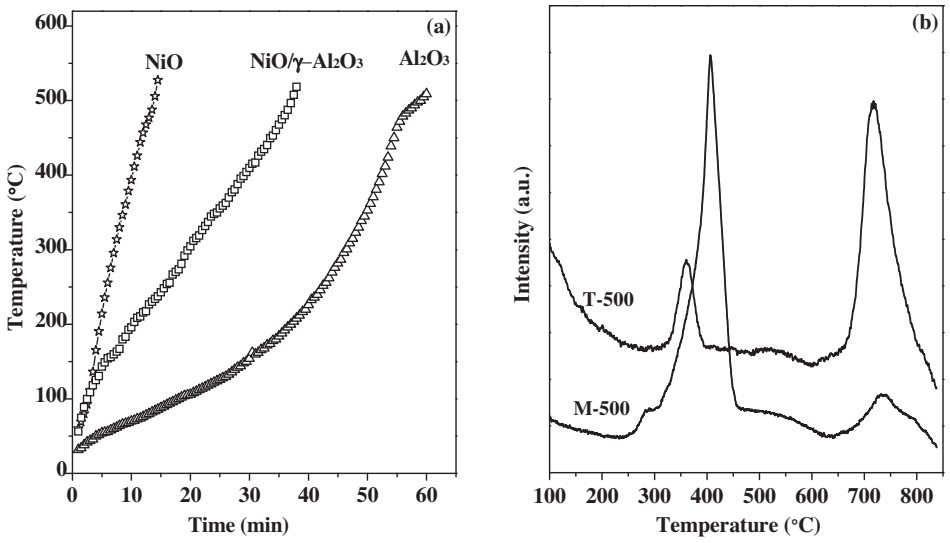

Fig. 9. (a) Microwave heating curve of various materials; (b) H_2-TPR profiles of T-500 and M-500 samples.

The crystal structure of alumina is another important factor that influences the formation of nickel species [60,61]. Alumina crystals can change from the γ- to α-type, with rapid decrease in specific surface area with increasing temperature [61]. Compared with γ-alumina, a weak interaction of the NiO species occurs on the α-alumina support.

Calcination temperature also plays an important role in the formation of NiO species in alumina-supported nickel catalysts. TPR results [37,49,62] show that the low-temperature peak area decreases rapidly with increasing calcination temperature and the interaction of Ni species with the alumina support becomes stronger at higher calcination temperatures. This occurs because easily reducible NiO species can be transformed into other Ni species that are difficult to reduce with increasing calcination temperature.

Li et al. [64] found that the reduction peaks of the H_2-TPR profiles shifted to lower temperature and the fraction of lower temperature peaks increased with increasing hydrothermal time. This occurs because hydration of the alumina support may result in a decrease in medium-strong and strong Lewis acid sites and is one of the reasons for the weakening of the Ni-support interaction.

4.1.2. Catalytic performance and influencing factors of amorphous NiO

Based on the H_2-TPR results, the NiO species were generally recognized as amorphous, dispersed crystal and fixed states in the alumina ($NiAl_2O_4$ phase) with increasing reduction temperature [18,19,22,35–42,53,54]. Amorphous NiO is easily reduced and displays high catalytic activity in many reactions because of its weak interaction with the alumina support [16–24,36–40,49,53–65]. In the methanation of CO or CO_2 [16–19,21,22], the formation of amorphous NiO species is promoted by additives, reducing the sintering temperature or improving the loading amount to achieve a high methane yield. The dehydrogenation activity can be improved by increasing the amount of amorphous NiO and reducing the interaction between surface NiO and the support in NH_3, hydrous hydrazine and ethanol dehydrogenation [36,40,62]. Moreover, increasing the hydrothermal time for the Ni/γ-Al_2O_3 catalyst could promote the formation of amorphous NiO and lead to improved catalytic performance in the hydrogenation of 1,4-butanediol [64].

To achieve improved catalytic performance, researchers have attempted to promote the formation of amorphous NiO in NiO/Al_2O_3 catalysts via various methods. However, hydrothermal synthesis is complex and time-consuming [64], and the amount of promoter is limited [18]. Furthermore, certain negative effects may result, such as a reduced surface area [16,22,62] and poor stability [49]. Therefore, the development of a simple and controllable method to promote the formation of amorphous NiO on the Ni/Al_2O_3 catalysts would be of great significance and useful in pursuing higher catalytic activity in related reactions.

In this study, the characterization results show that nickel species formed by the traditional and microwave heating methods are very different. Little amorphous NiO was formed with traditional heating. However, using simple operating conditions, we were able to synthesize large quantities of amorphous NiO rapidly by the microwave heating of Ni-Ce/Al_2O_3 catalysts. These catalysts showed high activity in the methanation of CO and CO_2. Moreover, the amount of amorphous NiO decreased gradually, while the strongly interacted NiO increased gradually with increasing nickel loading. Previous studies show that for Ni/Al_2O_3 catalysts prepared by the traditional heating method, amorphous NiO was formed more easily at higher nickel loading [36,37,53–56]. Therefore, these results may be attributed to the difference in heating mechanism under traditional and microwave heating conditions.

4.2. Formation mechanism of amorphous NiO species

NiO (prepared by the thermal decomposition of $Ni(NO_3)_2$ at 500 °C), γ-Al_2O_3, and NiO/γ-Al_2O_3 (NiO loading of 20%) were heated to 500 °C by microwave under the same conditions (3.5 kW) with the heating curves shown in Fig. 9(a). The ability to absorb microwave energy decreases according to NiO > NiO/Al_2O_3 > Al_2O_3. Therefore, the heating rate increases once Al_2O_3 is loaded with NiO and this is ascribed to the strong microwave-absorbing ability of NiO.

γ-Al_2O_3 powder (1.50 g) was made into a sheet of 20 mm diameter and 4 mm height, followed by mixing and compacting with NiO powder (5.00 g). The mixture was calcined for 1 h at 500 °C using a tube furnace and microwave (denoted as T-500 and M-500), respectively. The calcined samples were characterized by H_2-TPR analysis as shown in Fig. 9(b). The catalyst exhibits large reduction peaks of NiO at low temperature if heated by microwave and shifts to high temperature when heated in a tube furnace. This suggests that the solid-phase reaction capacity behaves differently for the two heating methods. According to previous analysis, it

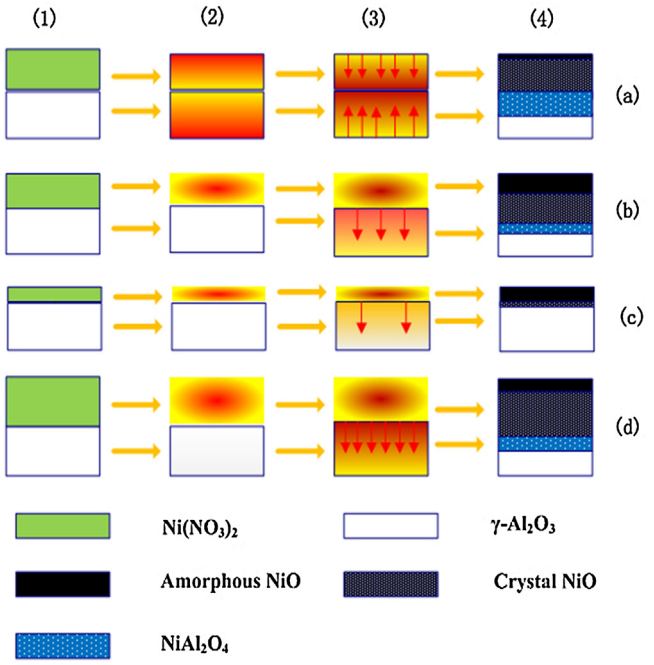

Fig. 10. Schematic model of the phase transformations in the samples at heating calcined process. (a) Traditional heating process; (b) microwave heating process; (c) low Ni-loading lever (microwave heating); and (d) higher Ni-lording lever (microwave heating).

is reasonable to assume that the sample, composed of a mixture of NiO and Al_2O_3, has a relatively weak solid-phase reaction ability under microwave, because variances in microwave absorption exist between the two materials. Hence, temperature differences emerge when they are heated to a certain value. This restrains NiO migration and depresses the interactions of NiO and Al_2O_3. In contrast, during tube furnace heating processes, Al_2O_3 imposes a slight resistance on NiO transfer, as a result stronger interactions result between them.

4.2.1. Traditional heating model

Fig. 10(a) shows a schematic diagram of the conventional heating process. Thermal energy is transmitted to matter by conduction, convection and radiation, so that the matter is heated from the outside inwards [66–68]. Nickel nitrate was decomposed to NiO and the γ-Al_2O_3 support was heated further by conventional conductive, convective and radiative heating [69]. It is worth noting that the catalyst is heated from the outside inwards [66,68].

As the temperature increases, thermal energy is conducted continuously to the generated NiO and support. This maintains a rapid increase in temperature for both. There was a minimal temperature difference between the alumina and surface NiO. The high-temperature support is also favorable for enhancing the interaction of the dissociative NiO with the support and improving the migration of NiO molecules into its inner part [36,37]. During the heating, NiO migrated into the alumina skeleton. As a result of the increase in migration loading, the content of migrated NiO in the skeleton gradually became saturated, and the distribution of NiO increased gradually from the inside to the surface [36,37]. As a result, a significant amount of surface NiO changed from the amorphous to an interaction state with the support, and part of the NiO migrated into the alumina skeleton, thereby forming a fixed state. A schematic diagram of the alumina-supported nickel catalyst obtained after conventional heat treatment is shown in Fig. 10(a)-(4).

4.2.2. Microwave heating model

Three qualitative categories exist in microwave heating for material classification with respect to its interaction with the electric field component of the microwave field: (i) in insulators, microwaves pass through without losses (transparent), (ii) in conductors, microwaves are reflected and cannot penetrate, and (iii) in absorbers, microwave energy is absorbed to a certain degree based on the value of the dielectric loss factor [70]. A fourth type of interaction is that of a mixed absorber. Mixed absorbers take advantage of one of the significant characteristics of microwave processing, that of selective heating. Microwaves are absorbed by a component with high dielectric loss while passing through a low loss material with little reduction in energy. In some processes and products, the heating of a specific component while ensuring the surrounding material remains relatively unaffected would be of great advantage. This selective heating process is not possible in conventional heating environments [71]. As for alumina-supported nickel catalysts, microwave heating leads to a noticeable result because of the difference in microwave-absorbing properties between nickel species and the alumina support.

Fig. 10(b) shows a schematic diagram of the microwave heating process. In the first stage, nickel nitrate, which is dispersed on the surface of the impregnated Ni/Al_2O_3 catalyst precursor, is decomposed to NiO with better dispersion by microwave irradiation heating. In the second stage, with further microwave heating, the generated NiO absorbs large amounts of microwave energy. However, as a poor absorber of microwaves at room temperature, alumina can absorb microwave energy more readily with increasing temperature. When the alumina temperature increases to 800 °C, it can absorb microwaves directly [68]. This results in a temperature gradient between the surface NiO and the bulk of the Al_2O_3 support, thereby limiting the migration of NiO inside the Al_2O_3 support. Meanwhile, heat is transferred from the surface NiO to the Al_2O_3 support [67]. As a result, the temperature of the surface-layer of the Al_2O_3 support is close to that of the NiO, and part of the NiO migrates into the surface layer of the support. Compared with the surface layer, minimal NiO entered into the support at lower temperature, as shown in Fig. 10(b)-(4).

Low Ni-loading: Fig. 10(c) shows a schematic diagram for the preparation of alumina-supported 5 wt% nickel catalysts (MO-5NC) by microwave heating. In the first stage, nickel nitrate dispersed on the surface of the Al_2O_3 support is decomposed rapidly to NiO, mainly because its microwave energy absorption results in a rapid increase in temperature under microwave heating. The generated NiO continues to absorb microwave energy and maintains an elevated temperature. Because of heat conduction, heat is transferred from the NiO surface to the inner part of the Al_2O_3 support [69]. Despite heat conduction, the support is not heated to a high temperature, because low nickel loading, which corresponds to low microwave energy absorption, means that less heat is transferred into the support. This is unfavorable for the migration of NiO molecules into the alumina skeleton. In fact, the presence of NiO in the alumina skeleton is at undetectable levels. Fig. 10(c)-(4) shows a schematic diagram of MO-5NC obtained after microwave heat treatment.

High Ni-loading: Fig. 10(d) shows a schematic diagram for the preparation of alumina-supported 20 wt% nickel catalyst (MO-20NC) by microwave heating. In the first stage, the reaction process is similar to that of Fig. 10(c). Compared with MO-5NC, a high nickel loading favors the absorption of a significant amount of microwave energy by NiO and thus more heat is transferred to the Al_2O_3 support. This results in a reduction in temperature gradient between the surface NiO and bulk of the Al_2O_3 support and the rate of NiO thermal movement into the support is accelerated. Moreover, the support with high temperature is helpful for the migration

of NiO into the alumina skeleton. In contrast with MO-5NC, the surface layer of MO-20NC has a lower amorphous NiO content, while the second NiO rich layer beneath the surface layer has a higher NiO content and strong interaction with the support. NiO that has migrated into the alumina skeleton exists mainly in the third layer, with an increase in the depth of the second layer as shown in Fig. 10(d).

5. Conclusion

A series of Ni-Ce/γ-Al_2O_3 catalysts was prepared by conventional and microwave heating methods and used for the methanation of simulated COG. The following conclusions can be drawn from this investigation:

(1) The conversion of CO and CO_2 increases with rise in temperature and pressure. In contrast, the overall trend of CO and CO_2 conversion is a gradual reduction with increase in weight hourly space velocity. Nevertheless, temperature is the most important factor in the methanation reaction. The MO-15NC catalyst shows optimal catalytic activity, with CO, CO_2, and O_2 being completely converted, as well as partial conversion of C_2H_6 using the following operating conditions: $T = 260\,^{\circ}C$, $P = 3.0$ MPa, and WHSV = 20000 mL g^{-1} h^{-1}.
(2) Characterization by XRD, H_2-TPR, H_2 pulse chemisorption, TPSR and TEM shows that microwave heating can promote the formation of amorphous NiO with weak interaction with the support, improve the degree of Ni dispersion and increase the active Ni surface area. This results in the improved catalytic performance of Ni-Ce/γ-Al_2O_3 catalysts in the methanation of CO and CO_2.
(3) The formation of amorphous NiO on the Ni-Ce/γ-Al_2O_3 catalysts is attributed to the selective heating behavior of different phases under microwave heating conditions. NiO, produced by the thermal decomposition of nickel nitrate, is heated through the absorption of large amounts of microwave energy; however, the alumina support does not absorb microwave energy below 800 °C. The temperature difference between NiO and alumina prevents the migration of NiO, resulting in the NiO existing partly as an amorphous state on the alumina support.
(4) Under conventional heating conditions, NiO and alumina are heated simultaneously at the same rate. This leads increasingly to a congregation of crystalline NiO with rise in temperature. As a result, large amounts of surface-dispersed crystal NiO and fixed $NiAl_2O_4$ were formed in the Ni-Ce/γ-Al_2O_3 catalysts.
(5) At higher nickel loadings, more microwave energy is absorbed by NiO and transformed to large amounts of heat energy as compared with low loadings. Large quantities of heat energy stored in the NiO are transferred to the alumina support, thereby decreasing their temperature difference. This results in a decrease in amount of amorphous phases, and more NiO species are presented in a form that interacts strongly with the alumina support.

Acknowledgments

This work has been supported by a Grant from the National Natural Science Foundation of China (21376159), the National Science Foundation for Post-doctoral Scientists of China (2014M551060), the National Basic Research Program of China (2012CB723100), the Natural Science Foundation of Shanxi Province (2010011014-5 and 2013011042-2) and the Key Science and Technology Program of Shanxi Province (20120313005-1).

References

[1] R. Razzaq, C. Li, S. Zhang, Fuel 113 (2013) 287.
[2] J.M. Bermúdez, B. Fidalgo, A. Arenillas, J.A. Menéndez, Fuel 89 (2010) 2897.
[3] Z. Yang, W. Ding, Y. Zhang, X. Lu, Y. Zhang, P. Shen, Int. J. Hydrogen Energy 35 (2010) 6239.
[4] Y. Zhang, Q. Li, P. Shen, Y. Liu, Z. Yang, W. Ding, X. Lu, Int. J. Hydrogen Energy 33 (2008) 3311.
[5] H. Zhu, R. Razzaq, L. Jiang, C. Li, Catal. Commun. 23 (2012) 43.
[6] J.M. Bermúdez, A. Arenillas, J.A. Menéndez, Int. J. Hydrogen Energy 36 (2011) 13361.
[7] J.M. Bermúdez, B. Fidalgo, A. Arenillas, J.A. Menéndez, Fuel 94 (2012) 197.
[8] H. Cheng, X. Lu, D. Hu, Y. Zhang, W. Ding, H. Zhao, Int. J. Hydrogen Energy 36 (2011) 528.
[9] W. Cheng, M. Lin, T. Leu, S. Du, Int. J. Hydrogen Energy 36 (2011) 11727.
[10] J.M. Bermúdez, A. Arenillas, R. Luque, J.A. Menéndez, Fuel Process. Technol. 110 (2013) 150.
[11] M. Onozaki, K. Watanabe, T. Hashimoto, H. Saegusa, Y. Katayama, Fuel 85 (2006) 143.
[12] W. Chen, M. Lin, A.B. Yu, S. Du, T. Leu, Int. J. Hydrogen Energy 37 (2012) 11748.
[13] G. Zhang, Y. Dong, M. Feng, Y. Zhang, W. Zhao, H. Cao, Chem. Eng. J. 156 (2010) 519.
[14] R. Razzaq, H. Zhu, L. Jiang, U. Muhammad, C. Li, S. Zhang, Ind. Eng. Chem. Res. 52 (2013) 2247.
[15] Y. Chen, in: D. Sherwood (Ed.), Development Strategies of the Chinese Natural Gas Market, Clingendael International Energy Programme, Hague, Netherlands, 2013.
[16] H. Liu, X. Zou, X. Wang, X. Lu, W. Ding, J. Nat. Gas Chem. 21 (2012) 703.
[17] A. Zhao, W. Ying, H. Zhang, H. Ma, D. Fang, J. Nat. Gas Chem. 21 (2012) 170.
[18] J. Gao, C. Jia, J. Li, M. Zhang, F. Gu, G. Xu, Z. Zhong, F. Su, J. Energy Chem. 22 (2013) 919.
[19] H. Zhang, Y. Dong, W. Fang, Y. Lian, Chem. Eng. J. 34 (2013) 330.
[20] J. Li, L. Zhou, P. Li, Q. Zhu, J. Gao, F. Gu, F. Su, Chem. Eng. J. 219 (2013) 183.
[21] S. Ma, Y. Tan, Y. Han, J. Nat. Gas Chem. 20 (2011) 435.
[22] A. Zhao, W. Ying, H. Zhang, H. Ma, D. Fang, Catal. Commun. 17 (2012) 34.
[23] J. Zhang, Y. Bai, Q. Zhang, X. Wang, T. Zhang, Y. Tan, Y. Han, Fuel 132 (2014) 211.
[24] G. Garbarino, P. Riani, L. Magistri, G. Busca, Int. J. Hydrogen Energy 39 (2014) 11557.
[25] S. Tada, R. Kikuchi, A. Takagaki, T. Sugawara, S.T. Oyama, K. Urasaki, S. Satokawa, Appl. Catal. B: Environ. 140–141 (2013) 258.
[26] M.A.A. Aziz, A.A. Jalil, S. Triwahyono, R.R. Mukti, Y.H. Taufiq-Yap, M.R. Sazegar, Appl. Catal. B: Environ. 147 (2014) 359.
[27] H. Yoshida, K. Watanabe, N. Iwasa, S. Fujita, M. Arai, Appl. Catal. B: Environ. 162 (2015) 93.
[28] I. Grac, L.V. González, M.C. Bacariza, A. Fernandes, C. Henriques, J.M. Lopes, M.F. Ribeiro, Appl. Catal. B: Environ. 147 (2014) 101.
[29] S. Tada, D. Minori, F. Otsuka, R. Kikuchi, K. Osada, K. Akiyama, S. Satokawa, Fuel 129 (2014) 219.
[30] C. Swalus, M. Jacquemin, C. Poleunis, P. Bertrand, P. Ruiz, Appl. Catal. B: Environ. 125 (2012) 41.
[31] J.N. Park, E.W. McFarland, J. Catal. 266 (2009) 92.
[32] K.P. Yu, W.Y. Yu, M.C. Kuo, Y.C. Liou, S.H. Chien, Appl. Catal. B: Environ. 84 (2008) 112.
[33] J. Ren, S. Liu, Z. Li, X. Lu, K. Xie, Appl. Catal. A: Gen. 366 (2009) 93.
[34] L.B. Råberg, M.B. Jensen, U. Olsbye, C. Daniel, S. Haag, C. Mirodatos, J. Catal. 249 (2007) 250.
[35] Y. Zhang, G. Xiong, S. Sheng, S. Liu, W. Yang, Acta Phys. Chim. Sin. 15 (1999) 735.
[36] J. Zhang, H. Xu, X. Jin, Q. Ge, W. Li, Appl. Catal. A: Gen. 290 (2005) 87.
[37] R. Yang, X. Li, J. Wu, X. Zhang, Z. Zhang, Y. Cheng, J. Guo, Appl. Catal. A: Gen. 368 (2009) 105.
[38] W. Zheng, J. Zhang, Q. Ge, H. Xu, W. Li, Appl. Catal. B: Environ. 80 (2008) 98.
[39] T. Borowiecki, W. Gac, A. Denis, Appl. Catal. A: Gen. 270 (2004) 27.
[40] L. He, Y. Huang, A. Wang, Y. Liu, X. Liu, X. Chen, J.J. Delgado, X. Wang, T. Zhang, J. Catal. 298 (2013) 1.
[41] L. Zhang, X. Wang, B. Tan, U.S. Ozkan, J. Mol. Catal. A: Chem. 297 (2009) 26.
[42] E. Heracleous, A.F. Lee, K. Wilson, A.A. Lemonidou, J. Catal. 231 (2005) 159.
[43] A.F. Trasarti, A.J. Marchi, C.R. Apesteguía, J. Catal. 247 (2007) 155.
[44] S. Lu, W.W. Lonergan, J.P. Bosco, S. Wang, Y. Zhu, Y. Xie, J.G. Chen, J. Catal. 259 (2008) 260.
[45] S. Hwang, J. Lee, U.G. Hong, J.C. Jung, D.J. Koh, H. Lim, C. Byun, I.K. Song, J. Ind. Eng. Chem. 18 (2012) 243.
[46] B.H. Sakakini, J. Mol. Catal. A: Chem. 127 (1997) 203.
[47] T. Bligaard, J.K. Nørskov, S. Dahl, J. Matthiesen, C.H. Christensen, J. Sehested, J. Catal. 224 (2004) 206.
[48] J. Yang, Y. Qi, J. Zhu, Y. Zhu, D. Chen, A. Holmen, J. Catal. 308 (2013) 37.
[49] S. Abelló, D. Verboekend, B. Bridier, J. Pérez-Ramírez, J. Catal. 259 (2008) 85.
[50] L. Zhang, J. Zhu, X. Jiang, D.G. Evans, F. Li, J. Phys. Chem. Solids 67 (2006) 1678.
[51] A.N. Mansour, Surf. Sci. Spectra 3 (1996) 239.
[52] L. Salvati, L.E. Makovsky, J.M. Stencel, F.R. Brown, D.M. Hercules, J. Phys. Chem. 85 (1981) 3700.
[53] Z. Hao, Q. Zhu, Z. Jiang, B. Hou, H. Li, Fuel Process. Technol. 90 (2009) 113.
[54] W. Wang, R. Ran, C. Su, Z. Shao, D.W. Jung, S. Seo, S.M. Lee, Int. J. Hydrogen Energy 36 (2011) 10958.

[55] Y. Kobayashi, J. Horiguchi, S. Kobayashi, Y. Yamazaki, K. Omata, D. Nagao, M. Konno, M. Yamada, Appl. Catal. A: Gen. 395 (2011) 129.
[56] L. Xu, H. Song, L. Chou, Appl. Catal. B: Environ. 108–109 (2011) 177.
[57] M.H. Amin, K. Mantri, J. Newnham, J. Tardio, S.K. Bhargava, Appl. Catal. B: Environ. 119–120 (2012) 217.
[58] T. Osaki, T. Mori, J. Catal. 204 (2001) 89.
[59] K.F.M. Elias, A.F. Lucrédio, E.M. Assaf, Int. J. Hydrogen Energy 38 (2013) 4407.
[60] A.L. Alberton, M.M.V.M. Souza, M. Schmal, Catal. Today 123 (2007) 257.
[61] M.L. Dieuzeide, V. Iannibelli, M. Jobbagy, N. Amadeo, Int. J. Hydrogen Energy 37 (2012) 14926.
[62] D.Z. Mezalira, L.D. Probst, S. Pronier, Y. Batonneau, C. Batiot-Dupeyrat, J. Mol. Catal. A: Chem. 340 (2011) 15.
[63] A. Iriondo, J.F. Cambra, M.B. Güemez, V.L. Barrio, J. Requies, M.C. Sánchez-Sánchez, R.M. Navarro, Int. J. Hydrogen Energy 37 (2012) 7084.
[64] H. Li, Y. Xu, C. Gao, Y. Zhao, Catal. Today 158 (2010) 475.
[65] X. Meng, H. Cheng, Y. Akiyama, Y. Hao, W. Qiao, Y. Yu, F. Zhao, S. Fujita, M. Arai, J. Catal. 264 (2009) 1.
[66] J. Zhou, C. Shi, B. Mei, R. Yuan, Z. Fu, J. Mater. Process. Technol. 137 (2003) 156.
[67] X. Zhang, D.O. Hayward, D.M.P. Mingos, Catal. Lett. 88 (2003) 33.
[68] Y. Fernández, A. Arenillas, J.Á. Menéndez, in: S. Grundas (Ed.), Advances in Induction and Microwave Heating of Mineral and Organic Materials. Part 31, InTech, Rijeka, Croatia, 2011, p. 725.
[69] X. Wu, Experimental and Theoretical Study of Microwave Heating of Thermal Runaway Materials, Virginia Polytechnic Institute and State University, 2002, pp. 3.
[70] W.H. Sutton, Am. Ceram. Soc. Bull. 68 (2) (1989) 376.
[71] D.E. Clark, D.C. Folz, J.K. West, Mater. Sci. Eng. A 287 (2000) 153.